High bandwidth nano-positioner: A robust control approach

S. Salapaka
Department of Mechanical and Environmental Engineering, UCSB, Santa Barbara, California 93106

A. Sebastian
Department of Electrical and Computer Engineering, Iowa State University, Ames, Iowa 50011

J. P. Cleveland
Asylum Research, 601-C Pine Avenue, Goleta, California 93117

M. V. Salapaka
Department of Electrical and Computer Engineering, Iowa State University, Ames, Iowa 50010

This article presents the design, identification, and control of a nano-positioning device suited to image biological samples as part of an atomic force microscope. The device is actuated by a piezoelectric stack and its motion is sensed by a linear variable differential transformer. It is demonstrated that the conventional proportional-integral control architecture does not meet the bandwidth requirements for positioning. The design and implementation of an H_∞ controller demonstrates substantial improvements in the positioning speed and precision, while eliminating the undesirable nonlinear effects of the actuator. The characterization of the resulting device in terms of bandwidth, resolution, and repeatability provided illustrates the effectiveness of the modern robust control paradigm. © *2002 American Institute of Physics.* [DOI: 10.1063/1.1499533]

I. INTRODUCTION

The advent of new techniques to explore properties of near atomic-scale structures has led to the development of the new field of nanotechnology. In the past decade, it has become evident that nanotechnology will make fundamental contributions to science and technology. Inevitably, most schemes of nanotechnology impose severe specifications on positioning. As is evident in scanning probe microscopy (SPM), which is one of the success stories of this new technology, precision in the order of angstroms is often desired. This demand for ultrahigh positioning precision forms a pivotal requirements in many applications of nanotechnology. For example, micro/nano-positioning systems are essential in auto focus systems,[1] fast mirror scanners, and image steering devices[2] in optics; disk spin stands and vibration cancellation in disk drives;[3–5] wafer and mask positioning in microelectronics;[6] micropumps,[7] needle valve actuation, linear drives, and piezo hammers[8] in precision mechanics; and cell penetration and microdispensing devices[9] in medicine and biology. Besides this requirement of high precision, there is also an increasing need for high bandwidth in such positioning systems. For example, in the field of cell biology, there are attractive proposals to employ nano-probes to track events in the cell. These events often have a time scale in the microsecond regimes. This necessitates high bandwidth positioning systems.

To meet the dual goal of high precision positioning at high bandwidth, novel sensors and actuators have been studied and developed. Most of the current high precision positioning devices utilize piezoelectric materials for actuation. The crystal lattices of these materials deform on the application of an electric field and these deformations are used for positioning with high accuracy. They achieve repeatable nanometer and subnanometer resolution at relatively high bandwidth since they have no sliding parts and thereby preclude undesirable effects such as backlash and stick–slip motions. Also, they can generate large forces (as high as few tens of kN), have very fast response times (acceleration rates of 10^4 g can be obtained), are not affected by magnetic fields, and are operable at wide ranges of temperatures (they are functional even at near zero Kelvin temperatures albeit with reduced sensitivity). Furthermore, they require very little power and no maintenance since they have no wear and tear.

However, the positioning is adversely affected due to nonlinearities such as hysteresis, especially when the piezo-actuators are used in relatively long range positioning applications. For instance, the maximum error due to hysteresis can be as much as 10%–15% of the path covered. Another detrimental effect is the drift due to creep. These effects become noticeable when piezoactuation is required over extended periods of time, i.e., during slow operation modes of the positioning device. Most of the commercially available open loop devices circumvent these nonlinear effects by using "harder" piezo ceramics. The nonlinear effects are smaller in these ceramics, but so is the travel generated.

In the recent past, some effort has been made to address these nonlinear effects. In Ref. 10, charge control (in contrast to voltage control) has been proposed to diminish the hysteresis effects. However, these techniques lead to increased drift and saturation problems and lead to further reduction of the travel range and the positioning bandwidth of the piezoactuator. In Ref. 11, postcorrection techniques for removing creep and hysteresis effects from SPM images have been presented. However, these postprocessing methods cease to

be useful for applications (such as cell biological studies) in which real time compensation is needed. In Ref. 12, the design of a feedback controller using an optical sensor attachment to a commercial atomic force microscope (AFM) to enhance its performance has been described. Another method utilized by commercial manufacturers is to restrict the motion to specific repetitive trajectories (e.g., raster scans) where the nonlinear effects can be compensated. In Ref. 13, the problem of nonlinear effects has been addressed by a careful identification/modeling of these nonlinearities and then using a model based inversion approach to compensate for the adverse effects. The efficacy of this approach depends on accuracy of modeling of the nonlinearities. However, this design methodology can be used in conjunction with the modern robust feedback control paradigm to achieve better performance and account for modeling uncertainties.

In this article, we present a nano-positioning device with a piezoelectric actuator and a linear variable differential transformer (LVDT) sensor. The device described here is an independent unit, and is not a modification or an enhancement of an already existing device. The architecture is motivated by applications to imaging biological samples where there is a need for an optical path through the sample. The piezoactuator used here is a stack piezo, in contrast to piezoelectric tube in Ref. 12 and Ref. 13. The stack piezos are cheaper and yield much larger forces and displacements when compared to tube piezos. In contrast to the tube piezo nanopositioner in use in most commercial scanning probe microscopes, the stack piezo based design has less coupling in the different directions of positioning. However, the nonlinear effects mentioned earlier are considerably more pronounced for the stack piezos. Another challenge imposed by the device architecture is the presence of right half plane zeros in the model of the system.

As indicated before, the attractive feature of piezo based positioning is the phenomenal achievable resolution. However, it is considerably difficult and impractical to fabricate sensors that can match the high resolution (particularly for high bandwidth applications) of the piezo based devices. Thus the feedback action, if not properly designed, can degrade the open loop positioning resolution considerably, thereby forfeiting one of the important features of the piezo based positioning.

On the other hand, the feedback action provides robustness and is a powerful mechanism to guarantee performance in the presence of nonlinearities and unmodeled dynamics that have a significant adverse effect in piezo based devices.

Unlike the tube piezo configuration [see Ref. 12 where the proportional-integral (PI) and the modern tools are compared for a tube piezo] where the well tuned traditional proportional-integral design can yield reasonable performance, the need for a framework to design controllers where the trade-off of the tracking bandwidth and the associated resolution is more acute for the stack based nanopositioning device presented here. This article illustrates the ineffectiveness of the traditional proportional-integral architecture used predominantly by the scanning probe community and provides a basis for such a judgment. In contrast, we show how the robust control framework allows for translating the per-
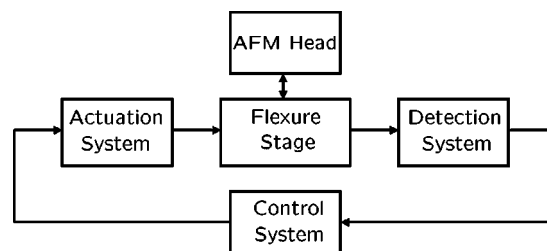

FIG. 1. Schematic block diagram of the device.

formance specifications (high bandwidth tracking, noise rejection) into an optimization problem that can be solved to obtain a controller meeting the specifications (if such a controller exists) in a methodical and streamlined manner. The implemented controller and the resulting nanopositioning device have considerably higher bandwidth (130 Hz, contrast to less than 3 Hz with the optimized PI control law).

This article is organized as follows. The description of the device and its design is presented in Sec. II. The identification of this model and the design of the feedback controllers to address the nonlinear effects are presented in Secs. III and IV, respectively. The resulting improvement in the performance of the device and its complete characterization in terms of its bandwidth, resolution, linearity, and travel range is presented in Sec. V. The comparison of performance with and without controllers is also presented in this section.

II. DEVICE DESCRIPTION

A schematic of the device is shown in Fig. 1. It consists of a flexure stage with a sample holder, an AFM head, an actuation system, a detection system, and a control system. The base plate [see Fig. 2(a)] is 20 cm × 20 cm×5 cm and is made of steel. From its center protrudes a cylindrical block for holding the sample. This part of the base plate that seats the sample holder executes the motion relative to its periphery. This motion is obtained by the serpentine spring design (see Fig. 3) where design grooves (about 150 μm wide) are cut in the base plate, making it possible for the flexure stage to move relative to the frame. The top plate sits on the base plate and is of similar dimensions as the base plate. It provides support for the AFM head above the sample [see Fig. 2(b)].
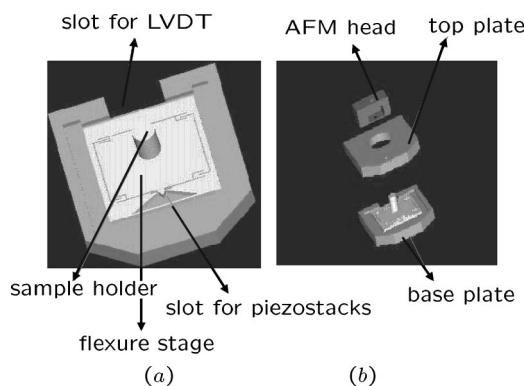

FIG. 2. (a) Base plate of the flexure stage. (b) Exploded view of the flexure and evaluation stages.
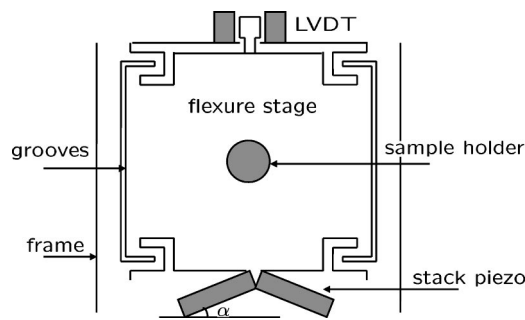
FIG. 3. Schematic describes the serpentine design for supporting the flexure stage. This figure is illustrative and not drawn to scale.

An AFM head is positioned above the sample holder so that AFM measurements can be simultaneously made with the LVDT measurements. Note that there is no Z piezo present, so the AFM is operating in what is known as "constant-height" mode. A basic schematic of the head is shown in Fig. 4. A laser beam is focused on the back of the cantilever near its free end and the reflected beam is directed onto a bi-cell photodetector. The resulting voltage signal is taken and processed to infer the topography of the surface.

The actuation system consists of a voltage amplifier and a piezo-stack arrangement shown in Fig. 5(a). This arrangement sits in the slot adjacent to the flexure stage [see Fig. 2(a)]. The amplified voltage signal applied across the piezo stack leads to its deformation which imparts the motion to the flexure stage. The input to the amplifier (which has gain of -15) is restricted to be negative and to be less than 10 V in magnitude since the piezo stack saturates beyond this limit. The piezo stacks are at an angle $\alpha \approx 7.5°$ [see Fig. 5(b)]. This arrangement, besides providing sufficient force to the flexure stage, also achieves a mechanical gain of $1/\sin(\alpha)$. If the piezo stacks have different gains, there is a possibility that the flexure stage is pushed out of the plane. The out-of-plane motion of the plate can, however, be detected by the AFM head. Experiments show that there was no appreciable out-of-plane motion.

The detection system consists of a LVDT and associated demodulation circuit. It has a resolution in the order of a few angstroms. The working principle of the LVDT is shown in Fig. 6(a). The excitation signal is a sinusoidal voltage with 14 V amplitude and 10 kHz frequency. It induces in the two secondary coils a sinusoidal voltage having the same frequency as excitation; however, the amplitude of the output varies with the position of the core. The core is attached to the moving flexure stage and the coils are attached to the stationary frame (see Fig. 3). When the secondaries are con-
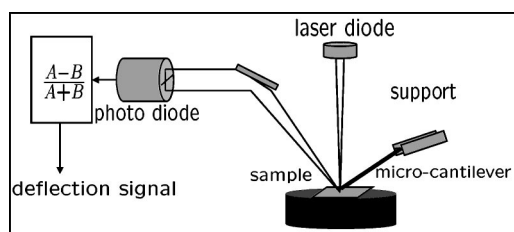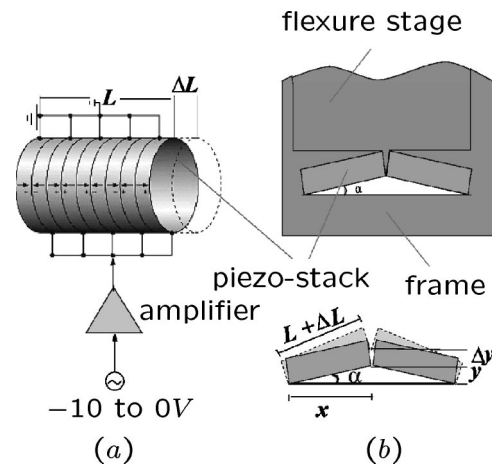

FIG. 5. Piezoactuation stage: (a) Actuation of a piezo stack. (b) Arrangement of the piezo stacks.

nected in opposition, there is a null position whose corresponding output is zero. In the apparatus, this null position has been adjusted so that it corresponds to the position of the flexure stage when an input of -5 V is given to the actuation system. Motion of the core from this null causes a larger mutual inductance on one coil and smaller on the other coil and the amplitude of the resulting output signal is a linear function of the core position for a considerable range on either side of the null. This amplitude modulated voltage signal is passed through a demodulation circuit to retrieve its amplitude. Thus, the output signal from the demodulation circuit is proportional to the motion of the flexure stage.

A block diagram of the control system is shown in Fig. 7. In the control algorithm, a reference signal (or the command signal) to be tracked is modified by a prefilter to regulate the bandwidth of the device by removing the high frequency content in the signal, and/or appropriately shaping the signal to achieve better tracking. The design of the prefilters and control laws is described in Sec. IV. These laws were implemented on a Texas Instruments C44 digital signal processor.

In this article, we denote the input to the actuation system by u, the demodulated output signal from the LVDT by y, and the system comprising the actuation, flexure, and detection stages by G. Also, we refer to u as the piezo input, y as the LVDT output, and G as the plant.

Figure 8 is a block diagram of the closed loop system. Here r represents the reference or the command signal; e
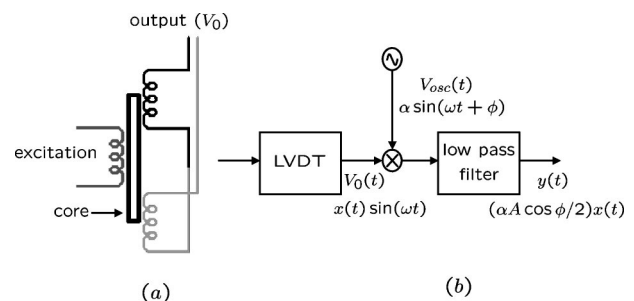

FIG. 4. A schematic of the evaluation stage.

FIG. 6. Detection stage: (a) Working principle of LVDT. (b) Demodulation of the amplitude modulated signal.

TI M44 DSP

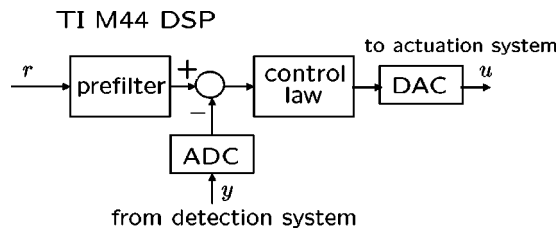FIG. 7. Schematic block diagram of the control system.

FIG. 9. Comparison of experimentally obtained and simulated frequency responses of the plant.

denotes the error signal, the difference between the reference and the output signals; and K stands for the controller transfer function. Also, we represent the open loop transfer function GK by L; the sensitivity function (the transfer function from r to e) by S; and the complementary sensitivity function (the transfer function from n to y by T.

III. IDENTIFICATION OF THE SYSTEM

The modeling of the device was done using the black-box identification technique where a specific point in the operating range of the device was chosen (where its behavior is approximately linear) and a model of the device at this point by studying its frequency response over a prespecified bandwidth was obtained. For this purpose, we used a HP 3563A signal analyzer, which gave a series of sinusoidal inputs, $u = -5 + A \sin(\omega t)$ (V), with frequencies spanning a bandwidth of 2 kHz. An offset of -5 V was given to operate the device about the null position. The amplitude, A, of the signals was chosen to be less than 50 mV so that the piezo response was approximately linear. The frequency response of the device at this operating point is shown by the Bode plot (dashed lines) in Fig. 9. A fourth order nonminimum phase transfer function

$$G(s) = \frac{9.7 \times 10^4 (s - (7.2 \pm 7.4i) \times 10^3)}{(s + (1.9 \pm 4.5i) \times 10^3)(s + (1.2 \pm 15.2i) \times 10^2)}$$

yielded a good fit to this data. Figure 9 shows the comparison between the frequency response data and the one simulated from the model, $G(s)$. The right hand plane (RHP) zeros of $G(s)$ need to be noted as they pose limitations on performance as described later.

This process was repeated to identify the system at different operating points (by giving various dc offsets) spanning the range of operation of the device. It was found that there was not much variation in the frequency responses (with $A \approx 50$ mV) at higher frequencies and the responses were slightly different in the dc range (see Fig. 10). There was considerable variation with respect to changes in the operating point of the frequency response when the sine sweep was done with large amplitude signals. However, we shall see in the next section that the robust feedback laws
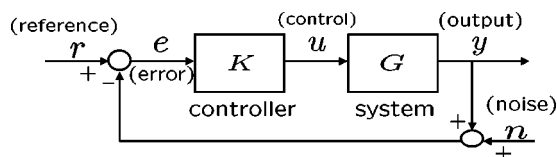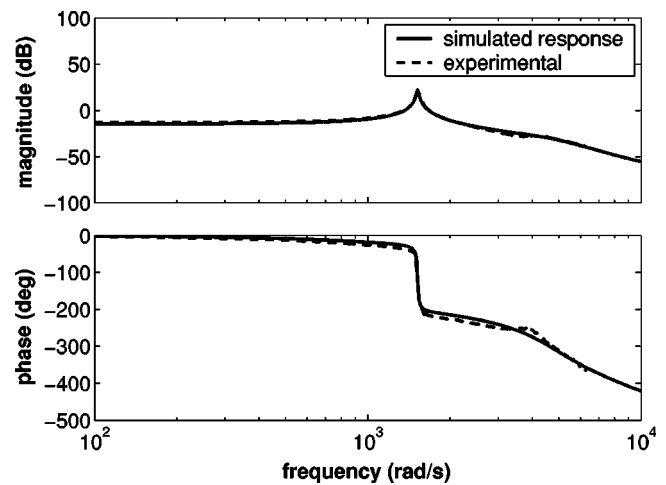
designed for the nominal plant (with the null position as the operating point) show persistent (robust) performance even with inputs having large amplitudes.

IV. CONTROL DESIGN

The model inferred for the device at the null operating point was employed to design the feedback laws. The primary objective of the control design is to achieve precise tracking of arbitrary input signals with high bandwidth. The feedback laws were constrained to provide control signals that were negative and within actuator saturation limits (-10 to 0 V). Besides these implementation constraints, the presence of RHP zeros impose fundamental constraints. From classical root locus analysis (see Refs. 14 and 15) we know that, as the feedback gain increases, the closed loop poles migrate to open loop zeroes, which implies high gain instability of the system. Hence high gain feedback laws are not applicable. They also impose a fundamental limit on the achievable bandwidth of the closed loop system. A complex pair of RHP zeroes, $z_{1,2} = x \pm iy$ (as in this case $z_{1,2} = (1.72 \pm 7.36i) \times 10^3$), the "ideal" controller leads to the following sensitivity function (see Refs. 15 and 16):

FIG. 8. Schematic block diagram of the closed loop system.
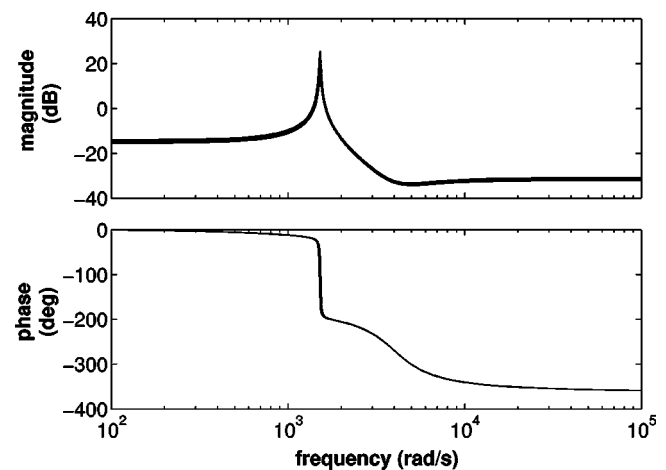
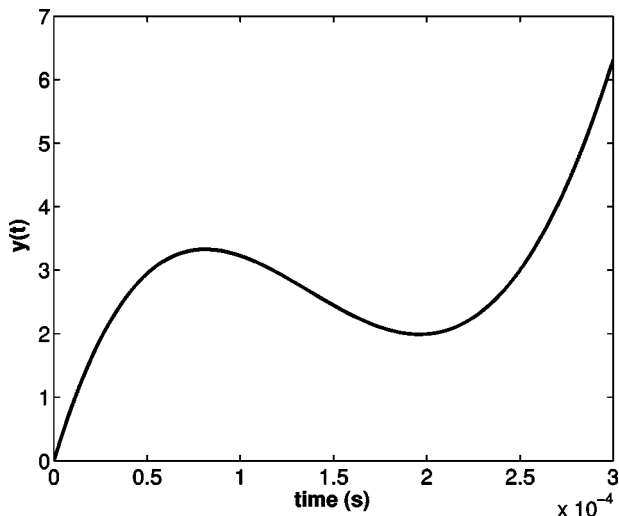FIG. 10. Frequency responses of the plant G at different operating points.

FIG. 11. Inverse response behavior of G to the impulse function. This indicates the presence of a pair of RHP zeroes.

$$S = \frac{4xs}{(s+x+jy)(s+x-jy)}.$$

By the above criteria the achievable bandwidth (the frequency at which $|S(j\omega)|$ crosses $-3dB$ from below) is approximately 415 Hz for the system. This controller is ideal in the sense, for a unit step reference $r(t)$, it generates an input $u(t)$ which minimizes the integral square tracking error

$$\int_0^\infty |y(t) - r(t)|^2 dt.$$

Note that such a controller might not be realizable (see Refs. 15 and 16).

Remark: It should be noted that flexible structures often show the inverse response behavior, i.e., the output initially decreases before increasing to its steady state value (in response to step or impulse given to the actuator). This behavior is also a characteristic of systems with RHP zeros (see the impulse response of the device in Fig. 11).

In industry, it is a common practice to design proportional (P) or proportional-integral (PI) controllers. In the next
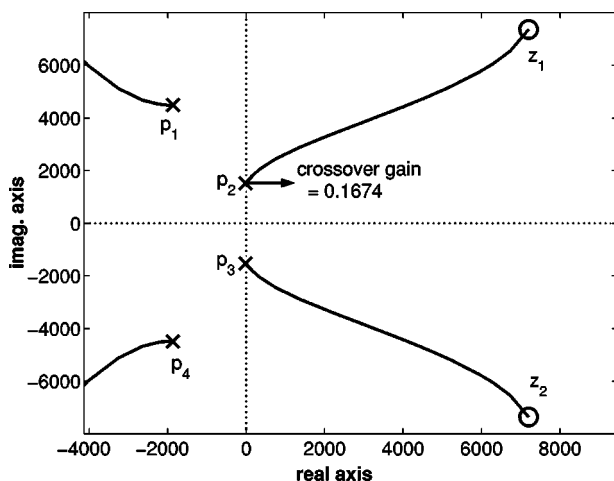

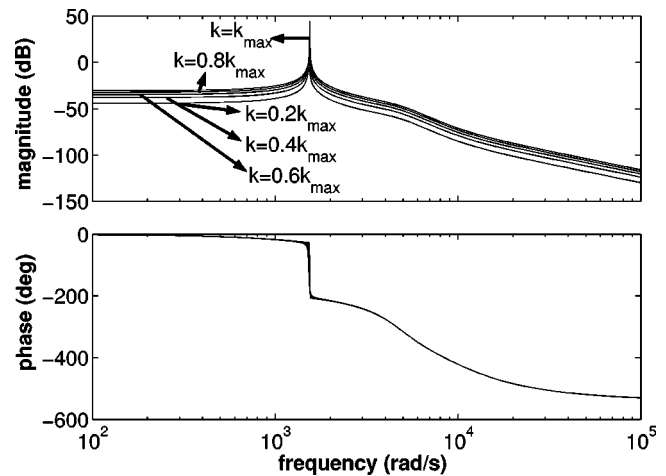FIG. 12. Root locus of the open loop transfer function, G.

FIG. 13. Bode plots of closed loop transfer function with different proportional controllers.

part of the article we show that this architecture is not suitable for the nanopositioning device presented.

1. Traditional control architecture: Proportional (P) and Proportional-Integral (PI) controller design

From the analysis of the root-locus plot of the open loop system, it is seen that the closed loop system is unstable for feedback gains greater tran 0.1674 (see Fig. 12). As is evident in Fig. 13, the gains at low frequency of the closed loop transfer function (for different proportional controllers ($0 < k < 0.1674$) are very low and hence the performance of the device is far from satisfactory.

If we assume a PI architecture ($k_p + k_i/s$) for the controller, we can determine the regions in the $k_p - k_i$ plane which guarantee closed loop stability [see Fig. 14(a)]. It should be noted that the region (in the $k_p - k_i$ plane) that gives high bandwidth [see plot (d)] is the region with low gain margin [see plot (c)]. Thus a trade-off between robustness and performance has to be decided. We chose $k_p = 0.01$ and $k_i = 75$, which guarantee a gain margin of 1.57
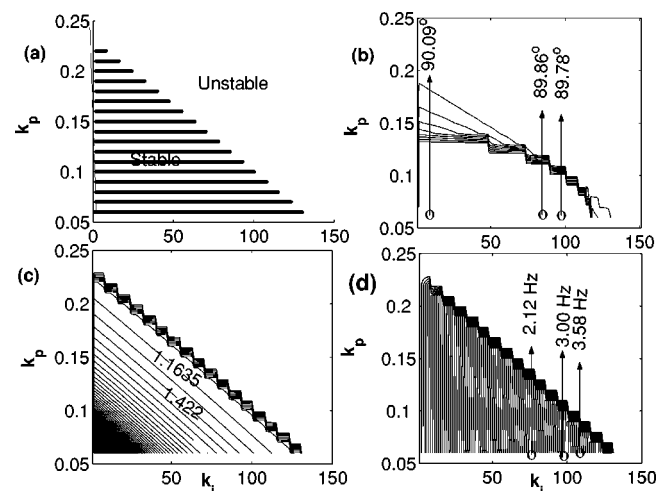

FIG. 14. (a) Region in $k_i - k_p$ plane that guarantees closed loop stability. Contour plots showing (b) phase margins, (c) gain margins, and (d) bandwidth of the closed loop systems corresponding to different points in the $k_i - k_p$ plane.
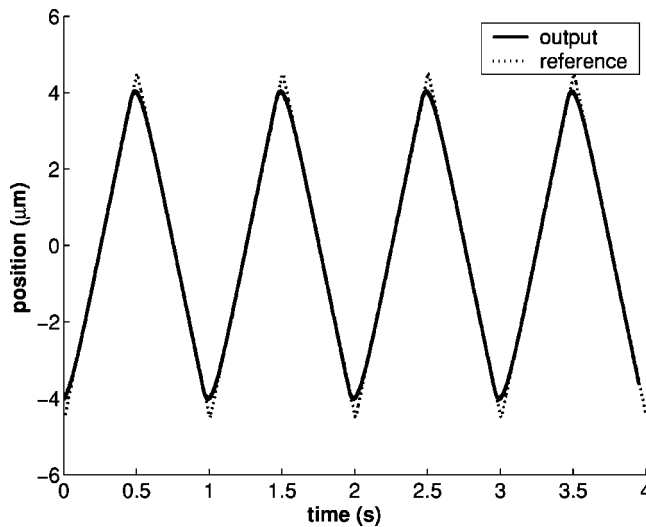
FIG. 15. Tracking of 1 Hz triangular signal with PI controller.

FIG. 16. (a) Generalized plant framework. (b) Closed loop system with regulated outputs.

and a phase margin of 89° and the corresponding bandwidth of the closed loop transfer function is 2.12 Hz. This controller was implemented and Fig. 15 shows tracking of a 1 Hz triangular wave. We see that there is good agreement between the reference and the LVDT-output signals for this input although the system has problems accurately tracking the sharp turn around.

It should be noted that the bandwidth (<3 Hz) attained with the PI architecture (the bandwidth can be slightly improved at the expense of robustness) is much less than the ideal bandwidth (≈ 415 Hz) as described in the previous section. This low bandwidth can be explained from the following simplified analysis. We approximate the plant G by considering only its slow modes $x+iy=(0.12\pm 15.2i)\times 10^2$ and ignoring the fast modes ($s(1.9\pm 4.5i)\times 10^3$). This results in a third order closed loop system whose characteristic polynomial is given by

$$s^3 + 2\,\delta\omega_n s^2 + (k_p + w_n^2)s + k_i,$$

where $\omega_n \triangleq \sqrt{x^2+y^2} = 15.2$ rad/s and $\delta \triangleq x/\omega_n = 8\times 10^{-3}$. For this system it can be shown that the bandwidth is in the order of $\delta\omega_n = 12$ rad/s $= 1.9$ Hz. This is in close agreement with the numerical analysis presented above.

The main reason for the failure of the PI design is that the poles of the closed loop system (even for the third order system) cannot be placed arbitrarily by choosing k_p and k_i. A higher order controller is needed to have full freedom in the placement of poles.

2. H_∞ controller design

The main advantage of using this design is that it includes the objectives of tracking and resolution in the problem formulation. More precisely, the control law is obtained as a solution to an optimization problem which incorporates the performance objectives like bandwidth and resolution in its cost function. This eliminates the tedious task of tuning the gains in the PI architecture (as illustrated later even the optimally tuned gains fail to yield acceptable performance).
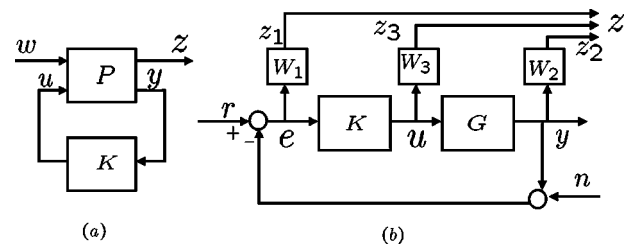
The first step towards H_∞ control design is to form the generalized plant, P. In the system [see Fig. 16(a)], the exogenous input w is the reference signal r, the control input is u and the measured output z is the error signal e. In order to reflect the performance objectives and physical constraints, the regulated outputs were chosen to be the weighted transfer function, $z_1 = W_1 e$, the weighted system output, $z_2 = W_2 y$, and the weighted control input, $z_3 = W_3 u$. The transfer function from w to z_1 is the weighted sensitivity function, $W_1 S$, which characterizes the performance objective of good tracking; the transfer function from $w=n$ to z_2 is the complementary sensitivity function, whose minimization ensures low control gains at high frequencies, and the transfer function from w to z_3 is KS, which measures the control effort. It is also used to impose the control signals to be within saturation limits. The weighting functions W_i, $i=1,2$, and 3 are used to scale these closed loop transfer functions to specify the frequency information of the performance objectives and system limitations. The inverse of the weighting functions is an upper bound (up to a constant scaling factor) on the transfer function it is used to scale.[15] The transfer function, W_1, is chosen such that it has high gains at low frequencies and low gains at high frequencies (see Fig. 17). This scaling ensures that the optimal feedback law is such that the sensitivity function is small at low frequencies, thus guaranteeing good tracking at the concerned frequencies. More precisely, W_1 was chosen to be a first order transfer function

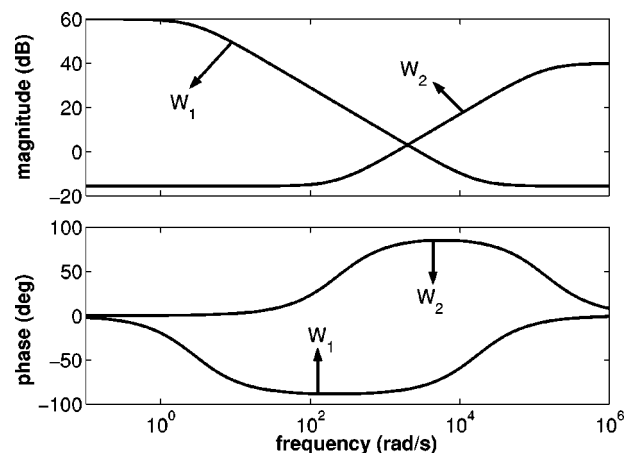$$W_1(s) = \frac{0.1667s + 2827}{s + 2.827}.$$

FIG. 17. Weighting transfer functions.

This transfer function is designed so that its inverse (an approximate upper bound on the sensitivity function) has a gain of 0.1% at low frequencies (<1 Hz) and a gain of ≈5% around 200 Hz.

The weighting function W_1 puts a low bound on the bandwidth of the closed loop system but does not allow us to specify the roll off of the open loop system to prevent high frequency noise amplification and to limit the bandwidth to be below Nyquist frequency. As already mentioned, piezoactuators do not have any backlash or friction and therefore have very fine resolution. The resolution of the device, therefore, depends on the experimental environment and it is limited by thermal and electronic noise. In any closed loop framework the high resolution of the piezoactuators may be compromised due the introduction of the sensor noise (in this case the LVDT) into the system. Clearly this effect is absent in the open loop case. In the H_∞ paradigm these concerns of sensor noise rejection are reflected by introducing a weighted measure of the complementary sensitivity function, T (which is the transfer function between the noise and the position y). In this case, this weight was chosen to be

$$W_2 = \frac{s+235.6}{0.01s+1414}$$

which has high gains at high frequencies (note that noise is in the high frequency region). There is another interesting interpretation of this weighting function. It decides the resolution of the device. Resolution is defined as the variance of the output signal y, when the device is solely driven by the noise n, i.e., resolution is equal to the variance of Tn. Thus, W_2 that guarantees lower roll off frequencies gives finer resolutions. In this way, the trade-off between conflicting design requirements of high bandwidth tracking (characterized by low $S, T \approx 1$) and fine resolutions (characterized by low T) is translated to the design of weighting transfer functions W_1 and W_2. The transfer function KS was scaled by a constant weighting $W_3 = 0.1$, to restrict the magnitude of the input signals such that they are within the saturation limits. This weighting constant gives control signals that are at most six times the reference signals.

In summary, the regulated outputs are given by

$$z = \begin{bmatrix} z_1 \\ z_2 \\ z_3 \end{bmatrix} = \begin{bmatrix} W_1(r-Gu) \\ W_2 Gu \\ W_3 u \end{bmatrix}$$

and the generalized plant P is described by

$$\begin{bmatrix} z \\ v \end{bmatrix} = \underbrace{\begin{bmatrix} \begin{bmatrix} W_1 & -W_1 G \\ 0 & W_2 G \\ 0 & W_3 \end{bmatrix} \\ [I-G] \end{bmatrix}}_{=P} \begin{bmatrix} r \\ u \end{bmatrix}.$$

In practice it is computationally simpler to design a suboptimal controller (i.e., one that is close to the optimal with respect to the H_∞ norm). In particular, for any $\gamma > \gamma_{opl} > 0$ we can find a controller transfer function K such that
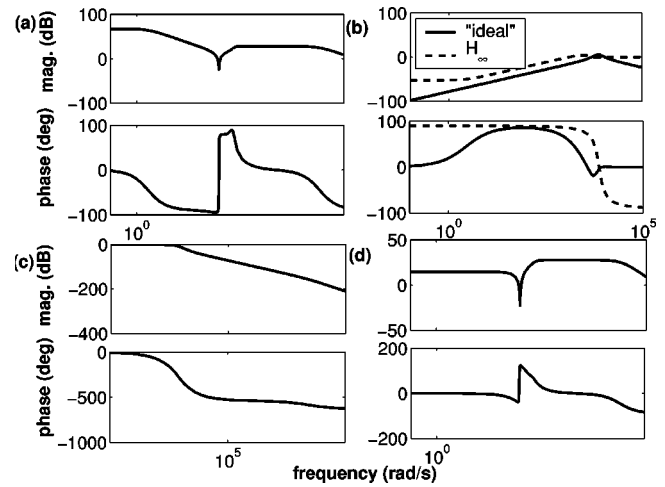

FIG. 18. Closed loop transfer functions: (a) controller, (b) sensitivity, (c) complementary sensitivity (d) KS.

$$\left\| \begin{bmatrix} W_1 S \\ W_2 T \\ W_3 KS \end{bmatrix} \right\|_\infty < \gamma,$$

where γ_{opt} is the optimal value. The controller was designed (using the function, hinfsyn in Matlab) for $\gamma = 2.415$ and the weighting functions described above. The following sixth order controller transfer function $K(s)$ was obtained with a dc gain of 2.2599×10^3, its poles at -1.14959×10^7, -1.4137×10^5, -5.6432×10^3, -2.8274, and $(-1.5676 \pm 5.8438i) \times 10^3$, and its zeroes at -1.4137×10^5, $(-1.8647 \pm 4.4958i) \times 10^3$, and $-1.1713 \times 10^1 \pm 1.5205i \times 10^3$.

The controller, the sensitivity, the complementary sensitivity function, and KS transfer functions are shown in Fig. 18. The bandwidth of the system (from the sensitivity transfer function) is found to be 138 Hz. It should be noted that this is an enormous improvement over the PI controller. Also, this controller provides a gain margin of 2.57 and a phase margin of 62.3° as opposed to the values of 1.57 and 89° in the PI controller. This shows that the robustness is considerably better with H_∞ controller. In this figure [plot (b)], we have compared the sensitivity function with the ideal one introduced earlier in the section.

The designed H_∞ controller was implemented and the resulting closed loop bandwidth was similar to that obtained theoretically. The performance of the H_∞ controller is significantly better than the PI controller (see Fig. 19).

Figure 20 shows the performance of this controller for a 25, 50, and 100 Hz triangular and 100 Hz reference signals. It can be seen that the closed loop system tracks the 25 and 50 Hz signals well [see plots (a) and (b)]. The mismatch in the case of the 100 Hz [in (c)] signal is due to the accentuation of higher modes of the triangular wave. In contrast, the 100 Hz sinusoidal signal shown in (d) does not have higher harmonics and the closed loop system shows much improvement in its tracking. In addition to the above advantages, the design process was capable of incorporating the engineering specifications in a streamlined manner in contrast to the often *ad hoc* way of tuning parameters in the PI design.
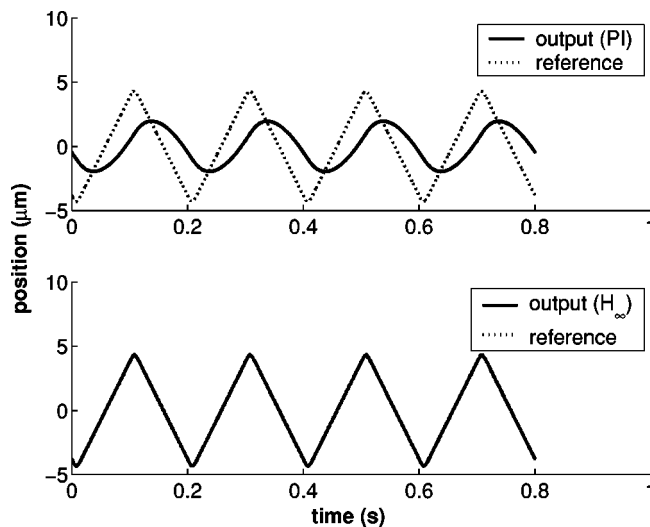
FIG. 19. Comparison of the performance of the closed loop system with (a) PI controller, (b) H_∞ controller.

V. CHARACTERIZATION OF THE DEVICE

In this section, we characterize the closed loop and the open loop device in terms of its resolution, bandwidth, and range. We also provide the comparison between PI and H_∞ designs. First, the device was calibrated using a calibration sample which had 180 nm high grooves every 5 μm. This grid was placed on the sample holder and probed by the AFM head. A triangular input of amplitude 2 V was given and the resulting LVDT output showed the presence of 7.26 grooves. This implies the device has a static sensitivity of 18.15 μm/V. It was seen that the input voltage of approximately 4 V can be given without reaching the limits of the actuator. This guarantees a travel range of 70 μm.

Elimination of nonlinear effects

The positioning precision of the piezoactuators is significantly reduced due to nonlinear effects such as hysteresis, drift, and creep. Hysteresis effects are significant when the
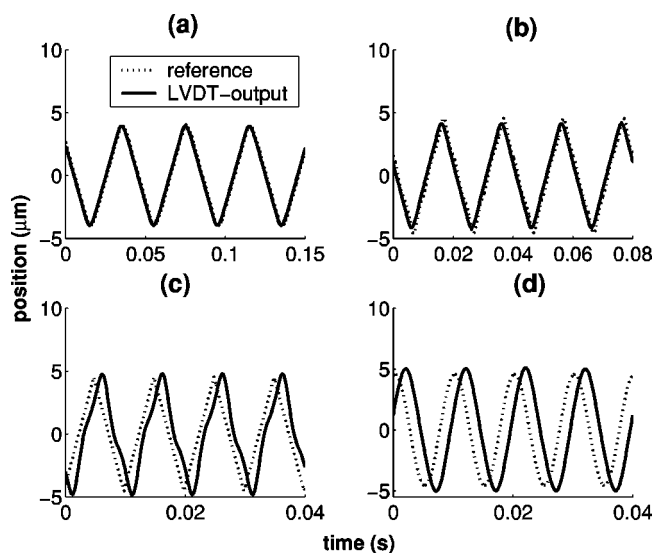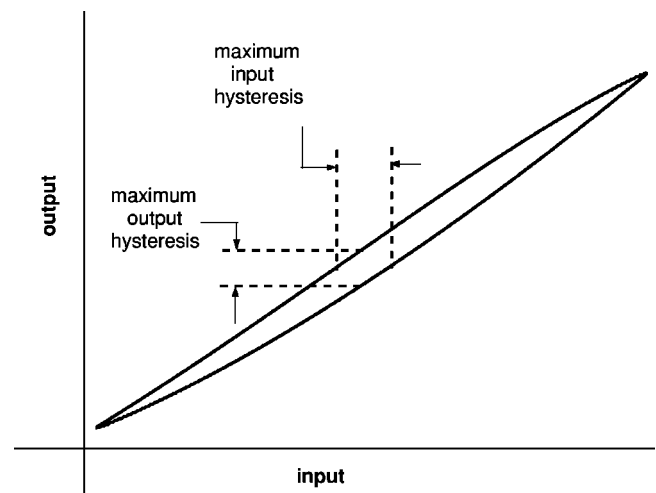

FIG. 21. Numerical quantification of hysteresis.

sensors are used for relatively long ranges. Therefore, open loop piezoactuators are typically operated in linear ranges to avoid positioning effects. However, with H_∞ design, these nonlinear effects are compensated and thus the closed loop device shows minimal hysteresis. To study this, we first plotted hysteresis curves by operating the device in open loop configuration and then compared them with the curves obtained by repeating the experiment in the closed loop configuration. Input signals (less than 1 Hz triangular pulses) of increasing amplitudes (1–4 V) were given in open loop configuration and the corresponding output signals recorded. The output versus reference plots are given in Fig. 22(a). It is observed that the hysteresis effects are dominant at higher amplitudes (longer travels). The hysteresis is quantified numerically in terms of maximum input (or output) hysteresis given as a percentage of the full scale (see Fig. 21). The maximum output hysteresis varies from 0.75 to 4.93 μm (7.2%–10% of corresponding travels) and the maximum input hysteresis varies from 0.14 to 0.73 V (5.8%–7.6% of drive inputs). A similar plot [see Fig. 22(b)] obtained for the closed loop configuration shows that the H_∞ design virtually eliminates all hysteretic effects. In this case, the travel length

FIG. 20. Tracking of (a) 25 Hz, (b) 50 Hz, (c) 100 Hz triangular waves, and (d) 100 Hz sinusoidal wave using the H_∞ controller.

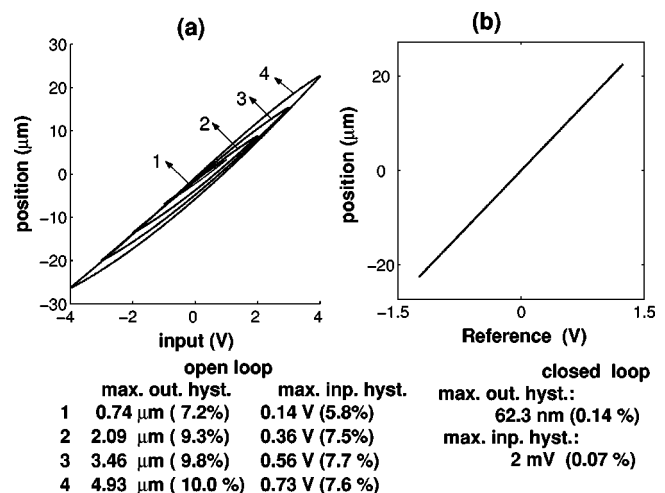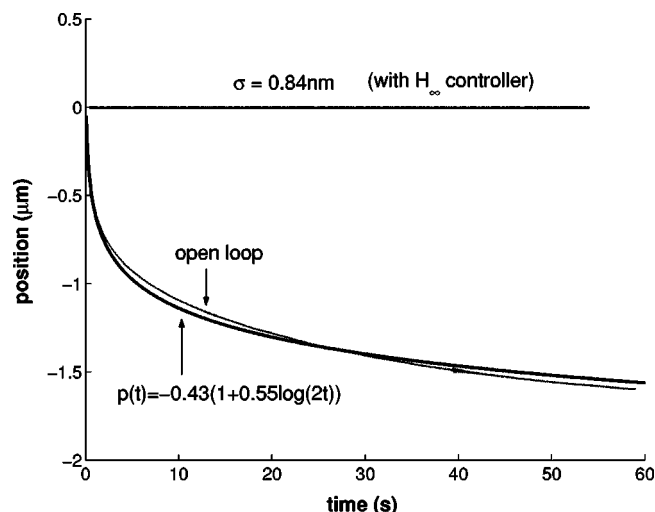|	open loop		closed loop
	max. out. hyst.	max. inp. hyst.	max. out. hyst.:
1	0.74 μm (7.2%)	0.14 V (5.8%)	62.3 nm (0.14 %)
2	2.09 μm (9.3%)	0.36 V (7.5%)	max. inp. hyst.:
3	3.46 μm (9.8%)	0.56 V (7.7 %)	2 mV (0.07 %)
4	4.93 μm (10.0 %)	0.73 V (7.6 %)	

FIG. 22. Hysteresis in (a) the open loop configuration, (b) its elimination in the closed loop configuration.

FIG. 23. Elimination of creep using H_∞ controller.

FIG. 25. (a) Reference (calibration sample) geometry. (b) Mismatch in the position of grooves between the forward and the backward traverses in the open loop. (c) Good match in the closed loop configuration.

is 45 μm and the maximum output hysteresis was significantly reduced to 62.3 nm (0.14%) and the corresponding maximum input hysteresis was reduced to 2 mV (0.07%).

Creep is another undesirable nonlinear effect common in piezoelectric actuators. It is related to the effect of the applied voltage on the remnant polarization of the piezo ceramics. If the operating voltage of a (open loop) piezoactuator is increased (decreased), the remnant polarization (piezo gain) continues to increase (decrease), manifesting itself in a slow creep (positive or negative) after the voltage change is complete. This effect is approximately described by the equation

$$y(t) \approx y_0[1 + \gamma \log(t/t_0)],$$

where t_0 is the time at which the creep effect is discernible, y_0 is the value of the signal at t_0, and γ is a constant, called the creep factor, that characterizes this nonlinear effect. To measure this effect, we studied the steady state step response of the device in open and closed loop configurations. The response $y(t)$ in the open loop was found to approximately

satisfy the creep law with a creep factor of 0.55. The same experiment conducted in the H_∞ closed loop (see Fig. 23) shows that the feedback laws virtually eliminate this effect and the system tracks the reference signal.

A significant adverse effect of the nonlinearities is that of nonrepeatability. This was seen clearly in the calibration experiment described in the previous section. In this case, the grooves that were observed when traveling in one direction were not concomitant with those in the other direction. This is shown in Fig. 24(a). The corresponding hysteresis curve is shown in Fig. 24(c). These effects were removed with H_∞ design and in Fig. 24(b), we see that the grooves in the forward and reverse directions are aligned with each other (The PI performance is not provided as the scan speed was well beyond the PI bandwidth). The corresponding hysteresis plot is shown in Fig. 24(d). The mismatch in the open loop is more clearly seen in Fig. 25(b), where the image obtained in one direction is positioned behind the one obtained in the other direction for the sake of comparison. In Fig. 25(c), the near perfect match with the H_∞ design is demonstrated. This nonrepeatability can lead to gross errors when the images are
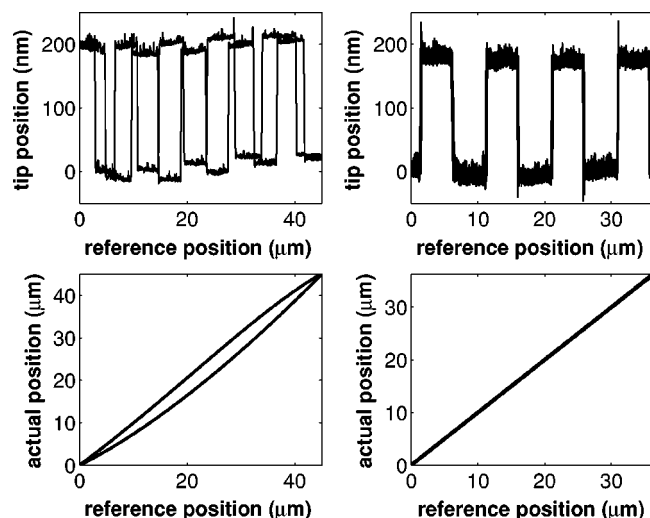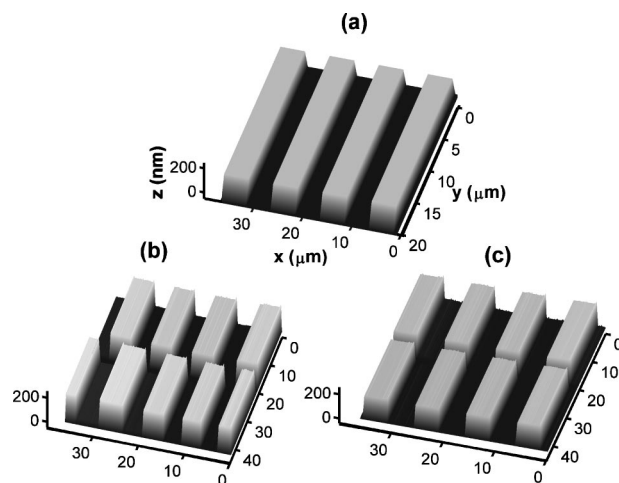

FIG. 24. Evaluation stage results: (a), (c) mismatch in the position of grooves between the forward and the backward traverses in the open loop and the corresponding hysteresis cycle. (b), (d) A good match in the closed loop configuration and the corresponding hysteresis cycle.
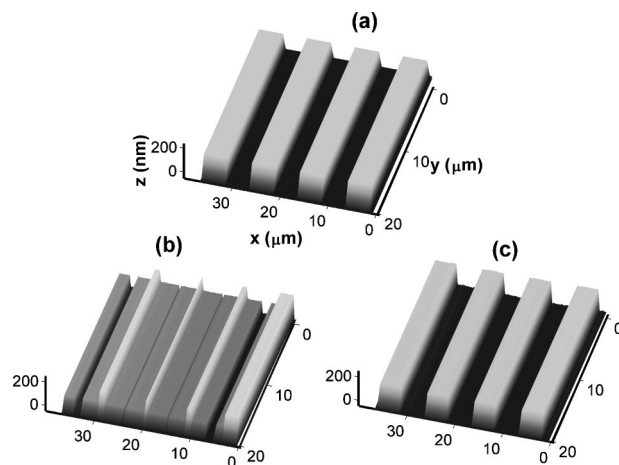

FIG. 26. (a) Calibration sample (top). (b) Distorted image obtained by averaged data in the open loop configuration (bottom left). (c) Faithful image obtained by averaging in the closed loop (bottom right).

averaged over many scans (say to remove the effects of noise). For example, the plot in Fig. 26 (bottom left) shows the scan of grooves obtained by averaging over the forward and the backward directions. It can be seen that it has no semblance with the actual calibration sample (top). However, the averaged scan in the closed loop case (bottom right), matches very well with the sample.

[1] Z. Rihong, D. X. Y. Zhixing, and C. Jinbang, Proc. SPIE **3553**, 297 (1988).

[2] D. Krogmann, H. D. Tholl, P. Schreiber, A. Krehl, R. Goring, B. Gotz, and Th. Martin, in 3rd International Conference on Micro Opto Electro Mechanical Systems, MOEMS 99, Mainz, Germany, 1999, pp. 178–185.

[3] M. Jianxu and M. Ang, Jr., Proc. SPIE **4194**, 94 (2000).

[4] Z. Wang, W. Zhu, C. Zhao, and X. Yao, IEEE Trans. Ultrason. Ferroelectr. Freq. Control **48**, 1103 (2001).

[5] W. Zhu, Z. Wang, X. Sun, and Z. Zhan, J. Mater. Sci. **12**, 111 (2001).

[6] D. White and O. Wood, J. Vac. Sci. Technol. B **18**, 3552 (2001).

[7] D. Xinfang and L. Yanhai, IEEE Trans. Electron Devices **24**, 87 (2001).

[8] C. Lee, C. Lin, C. Hsia, and W. Liaw, J. Guid. Control Dyn. **21**, 692 (1998).

[9] D. Meldrum *et al.*, in Proceedings of 2001 IEEE/ASME International Conference on Advanced Intelligent Mekatronics, 2001, Vol. 2, pp. 1211–1219.

[10] H. Kaizuka, Rev. Sci. Instrum. **60**, 3119 (1989).

[11] R. Barrett and C. Quate, Rev. Sci. Instrum. **62**, 1393 (1991).

[12] A. Daniele, S. Salapaka, M. Salapaka, and M. Dahleh, in Proceedings of the American Control Conference, San Diego, CA, 1999, pp. 253–257.

[13] D. Croft, G. Shedd, and S. Devasia, in Proceedings of the American Control Conference, Chicago, IL, 2000, pp. 2123–2128.

[14] G. Franklin, J. Powell, and A. Emami-Naeni, *Feedback Control of Dynamic Systems* (Addison–Wesley, Reading, MA, 1986).

[15] S. Skogestad and I. Postlethwaite, *Multivariable Feedback Control, Analysis and Design* (Wiley, New York, 1997).

[16] M. Morari and E. Zafiriou, *Robust Process Control* (Prentice–Hall, Englewood Cliffs, NJ, 1989).